universe

MDPI

Article

Astroparticle Constraints from the Cosmic Star Formation Rate Density at High Redshift: Current Status and Forecasts for JWST

Giovanni Gandolfi [1,2,3,*], Andrea Lapi [1,2,3,4], Tommaso Ronconi [1,2] and Luigi Danese [1,2]

1 Scuola Internazionale Superiore Studi Avanzati (SISSA), Physics Area, Via Bonomea 265, 34136 Trieste, Italy
2 Institute for Fundamental Physics of the Universe (IFPU), Via Beirut 2, 34014 Trieste, Italy
3 Istituto Nazionale Fisica Nucleare (INFN), Sezione di Trieste, Via Valerio 2, 34127 Trieste, Italy
4 Istituto di Radio-Astronomia (IRA-INAF), Via Gobetti 101, 40129 Bologna, Italy
* Correspondence: ggandolf@sissa.it

Abstract: We exploit the recent determination of the cosmic star formation rate (SFR) density at high redshifts $z \gtrsim 4$ to derive astroparticle constraints on three common dark matter (DM) scenarios alternative to standard cold dark matter (CDM): warm dark matter (WDM), fuzzy dark matter (ψDM) and self-interacting dark matter (SIDM). Our analysis relies on the ultraviolet (UV) luminosity functions measured from blank field surveys by the Hubble Space Telescope out to $z \lesssim 10$ and down to UV magnitudes $M_{\rm UV} \lesssim -17$. We extrapolate these to fainter yet unexplored magnitude ranges and perform abundance matching with the halo mass functions in a given DM scenario, thus, obtaining a redshift-dependent relationship between the UV magnitude and the halo mass. We then computed the cosmic SFR density by integrating the extrapolated UV luminosity functions down to a faint magnitude limit $M_{\rm UV}^{\rm lim}$, which is determined via the above abundance matching relationship by two free parameters: the minimum threshold halo mass $M_{\rm H}^{\rm GF}$ for galaxy formation, and the astroparticle quantity X characterizing each DM scenario (namely, particle mass for WDM and ψDM, and kinetic temperature at decoupling T_X for SIDM). We perform Bayesian inference on such parameters using a Monte Carlo Markov Chain (MCMC) technique by comparing the cosmic SFR density from our approach to the current observational estimates at $z \gtrsim 4$, constraining the WDM particle mass to $m_X \approx 1.2^{+0.3\,(11.3)}_{-0.4\,(-0.5)}$ keV, the ψDM particle mass to $m_X \approx 3.7^{+1.8\,(+12.9.3)}_{-0.4\,(-0.5)} \times 10^{-22}$ eV, and the SIDM temperature to $T_X \approx 0.21^{+0.04\,(+1.8)}_{-0.06\,(-0.07)}$ keV at 68% (95%) confidence level. Finally, we forecast how such constraints will be strengthened by upcoming refined estimates of the cosmic SFR density if the early data on the UV luminosity function at $z \gtrsim 10$ from the James Webb Space Telescope (JWST) will be confirmed down to ultra-faint magnitudes.

Keywords: dark matter; galaxy formation

Citation: Gandolfi, G.; Lapi, A.; Ronconi, T.; Danese, L. Astroparticle Constraints from the Cosmic Star Formation Rate Density at High Redshift: Current Status and Forecasts for JWST. *Universe* **2022**, *8*, 589. https://doi.org/10.3390/universe8110589

Academic Editor: Gonzalo J. Olmo

Received: 6 October 2022
Accepted: 4 November 2022
Published: 7 November 2022

1. Introduction

Astrophysical and cosmological probes have firmly established that baryons constitute only some 15% of the total matter content in the Universe. The rest is in the form of 'dark matter' (DM), which interacts very weakly or negligibly with the baryons except via long-range gravitational forces. However, no firm detection of DM particles has been made so far, despite the big efforts carried on with colliders [1–3] or with direct [4,5] and indirect [6–9] searches in the sky.

The standard lore envisages DM to be constituted by weakly interacting particles with masses of order GeV [10] that are non-relativistic at the epoch of decoupling (hence they are dubbed 'cold' dark matter or CDM) and feature negligible free-streaming velocities (i.e., they do not diffuse out of perturbations before collapse). As a consequence, bound CDM structures called halos to grow sequentially in time and hierarchically in mass by stochastically merging together [11,12].

On the cosmological scale, the CDM hypothesis is remarkably consistent with the data [13], while on (sub)galactic scales, it faces some challenges. For example, with respect to the predictions of gravity-only N-body simulations, the shape of the inner density profiles in DM-dominated dwarfs is too flat [14,15], and the number and dynamical properties of observed Milky Way satellites differ from those of subhalos [16,17]. Moreover, the emergence of tight empirical relationships between properties of the dark and luminous components in disc-dominated galaxies, such as the universal core surface density or the radial acceleration relation [18,19], seems to be indicative of a new dark sector and/or of non-gravitational coupling between DM particles and baryons. Although the above effects can, in principle, be explained in CDM by invoking physical processes that cause transfer of energy and angular momentum from baryons to DM particles, such as dynamical friction [20,21] or feedback effects from stars and active galactic nuclei [22–24], a fine-tuning is required to explain in detail the current data.

This has triggered the consideration of alternative, and perhaps more fascinating, solutions that rely on non-standard particle candidates [25–29]. The most widespread scenarios in the literature, which are also relevant for the present work, include warm dark matter (WDM) particles with masses in the keV range [30,31]; fuzzy or particle-wave dark matter (ψDM), constituted by ultralight axion-like particles with masses $\gtrsim 10^{-22}$ eV [32,33]; self-interacting dark matter (SIDM) with masses in the range $\sim 10 - 250$ MeV, as required by the cross-section $\sigma_{XX}/m_X \sim 0.1 - 1$ cm^2 g^{-1} estimated from clusters to galaxies [34,35]. As a consequence of free-streaming, quantum pressure effects, and/or dark-sector interaction, all these scenarios produce a matter power spectrum suppressed on small scales, fewer (sub)structures, and flatter inner density profiles within halos relative to CDM [36–43]. Indirect astrophysical constraints on the properties of such non-standard DM scenarios have been obtained by investigating the Lyman-α forest [44–47], high-redshift galaxy counts [48–51], γ-ray bursts [52,53], cosmic reionization [54–58], gravitational lensing [59,60], integrated 21 cm data [61–64], γ-ray emission [65,66], fossil records of the Local Group [67,68], dwarf galaxy profiles and scaling relations [69,70], and Milky Way satellite galaxies [71–75] or a combination of these [76].

The present paper will focus on the constraints to DM that can be derived from recent observations of the cosmic SFR density at high redshift $z \gtrsim 4$ (e.g., [77–80]). This observable crucially depends on the number density of ultra-faint galaxies, which tend to live within small halos, and especially so at high redshifts. Thus, their numbers can constrain the shape of the halo-mass distribution and of the power spectrum at the low-mass end, which is sensitive to the microscopic properties of the DM particles. With respect to other probes of DM exploited in the literature, the cosmic SFR density is a very basic astrophysical quantity that suffers less from observational, systematic, and modeling uncertainties.

More in detail, we build up an empirical model based on the UV luminosity functions measured from blank-field surveys by the Hubble Space Telescope up to $z \lesssim 10$ and UV magnitudes $M_{\rm UV} \lesssim -17$. We extrapolate these to fainter yet unexplored magnitudes, and perform abundance matching with the halo mass functions in a given DM scenario, so obtaining a redshift-dependent relationship between the UV magnitude and the halo mass. We then computed the cosmic SFR density by integrating the extrapolated UV luminosity function down to a faint magnitude limit $M_{\rm UV}^{\rm lim}$, which is determined via the above abundance matching relationship by two free parameters describing our astrophysical and astroparticle uncertainties: the minimum threshold halo mass $M_{\rm H}^{\rm GF}$ for galaxy formation, and a quantity X specific to each DM scenario (e.g., WDM particle mass). We perform Bayesian inference on the two parameters $M_{\rm H}^{\rm GF}$ and X via a standard MCMC technique by comparing the cosmic SFR density from our approach with the current observational estimates at $z \gtrsim 4$. Finally, we forecast how the constraints on these parameters will be strengthened by upcoming refined estimates of the cosmic SFR density at $z \gtrsim 10$ if the early data on the UV luminosity function from the James Webb Space Telescope (JWST) will be confirmed down to ultra-faint magnitudes.

The structure of the paper is straightforward: in Section ,2 we describe our methods and analysis; in Section ,3 we present and discuss our results; in Section ,4 we summarize our findings and highlight future perspectives. Throughout the work, we adopt the standard, flat cosmology [13] with rounded parameter values: matter density $\Omega_M \approx 0.31$, baryon density $\Omega_b \approx 0.05$, Hubble constant $H_0 = 100\,\mathrm{h\ km\ s^{-1}\ Mpc^{-1}}$ with $h \approx 0.68$. A Chabrier [81] initial mass function (IMF) is assumed.

2. Methods and Analysis

We start from the recent determination of the UV luminosity functions by [77,78] down to the redshift $z\sim10$ and UV magnitudes $M_{\rm UV} \lesssim -17$. In Figure ,1 we illustrate the binned luminosity functions (filled circles) at $\approx$ 1600 Å in the relevant redshift range $z\sim6$–10 (color-coded), together with the corresponding continuous Schechter function rendition (solid lines) in the form

$$\frac{\mathrm{d}N}{\mathrm{d}M_{\rm UV}\,\mathrm{d}V} = \phi^\star\,\frac{\ln(10)}{2.5}\,10^{-0.4\,(M_{\rm UV}-M^\star_{\rm UV})\,(\alpha+1)} \times e^{-10^{-0.4\,(M_{\rm UV}-M^\star_{\rm UV})}} \quad (1)$$

We characterize the evolution with redshift of the parameters entering Equation (1) according to the expressions by [78,79]. Toward high z, these yield a steepening faint end-slope $\alpha \approx -1.95 - 0.11\,(z-6)$, an approximately constant characteristic magnitude $M^\star_{\rm UV} \approx -21.04 - 0.05\,(z-6)$ and an appreciably decreasing normalization $\phi^\star \approx 3.8\times10^{-4-0.35\,(z-6)-0.027\,(z-6)^2}$ Mpc^{-3}. In Figure 1, we also report the intrinsic luminosity functions after correction for dust extinction (dotted lines), which have been computed exploiting the relation between extinction, the slope of the UV spectrum, and observed UV magnitude by [82,83]; the effects of dust extinction on the UV luminosity function are minor for $M_{\rm UV} \gtrsim -17$, and will be irrelevant for this work. The intrinsic UV luminosity can be related to the physical SFR of galaxies; in particular, for a Chabrier IMF, age $\gtrsim 10^8$ years, and appreciably sub-solar metallicity the relation log SFR [M$_\odot$ year^{-1}] $\approx -0.4\,(M_{\rm UV}+18.5)$ holds (see [84–88]), and the related values are reported on the top axis in Figure 1.

In Figure 1, we also report two other sets of data. The first one (open circles) is from [79], which has been able to estimate the luminosity function down to $M_{\rm UV} \approx -12.5$ by exploiting gravitational lensed galaxies in the Hubble Frontier Field clusters. However, the considerable statistical uncertainties related to the paucity of detected sources and the possible systematics in the lensing reconstruction and completeness issues do not yet allow us to draw firm conclusions on the shape of the luminosity function at such ultra-faint magnitudes. The second set of data (filled squares) involves the early results of JWST by [80], which have provided an estimate of the luminosity function at $z \gtrsim 12$, though with rather low statistics. Interestingly, it seems that at $z\sim12$, the shape of the luminosity function is roughly consistent with the lower redshift estimates, though its evolution in normalization considerably slows down; more data are needed to confirm such a trend, which could be very relevant for the astroparticle constraints of this work, as we will show and forecast.

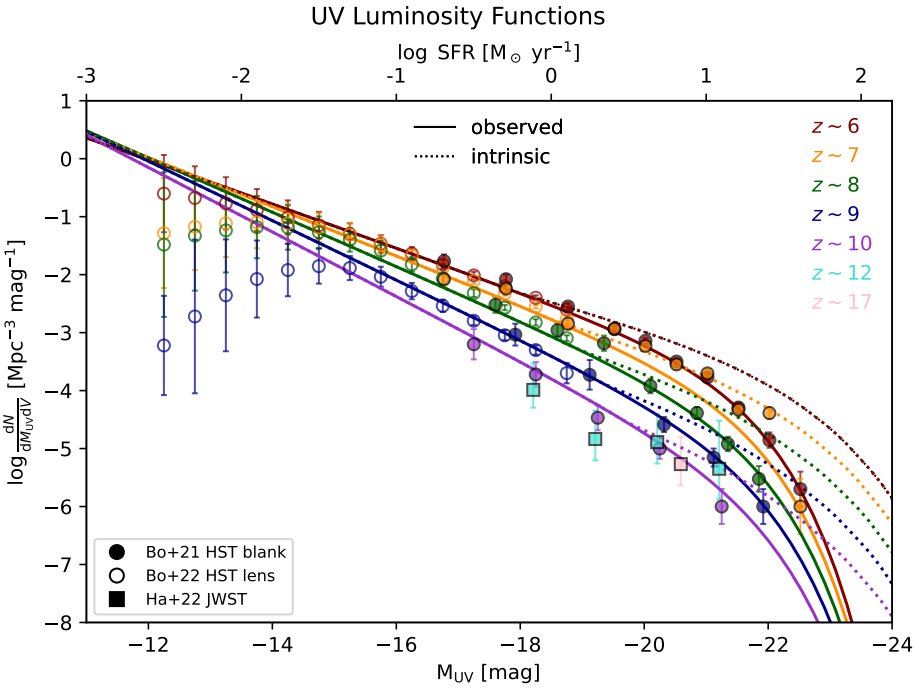

Figure 1. The UV luminosity functions at redshifts $z\sim6$ (red), 7 (orange), 8 (green), 9 (blue), 10 (magenta), 12 (cyan) and 17 (pink). Data points are from [77,78] (filled circles), [79] (empty circles), and [80] (squares). Colored lines illustrate Schechter fits the blank-field measurements from [78]: solid lines refer to the observed luminosity functions, while dotted lines to the intrinsic ones, after correction for dust extinction via the UV continuum slope according to the procedure by [83].

From the intrinsic UV luminosity functions, the cosmic SFR density can be computed as

$$\rho_{\rm SFR}(z) = \int_{-\infty}^{\min[M_{\rm UV}^{\rm obs}, M_{\rm UV}^{\rm lim}]} {\rm d}M_{\rm UV} \, \frac{{\rm d}N}{{\rm d}M_{\rm UV}\,{\rm d}V} \, {\rm SFR}\,, \tag{2}$$

where $M_{\rm UV}^{\rm obs}$ is the faintest limit probed by observations (e.g., $M_{\rm UV} \approx -13$ for [79], or ≈ -17 for [80]), and $M_{\rm UV}^{\rm lim}$ represents a limiting magnitude down to which the luminosity function is steeply increasing, i.e., we consider that the SFR density is negligible, contributed by magnitudes $M_{\rm UV} \gtrsim M_{\rm UV}^{\rm lim}$ fainter than such a limit. The quantity $M_{\rm UV}^{\rm lim}$ is somewhat uncertain: as mentioned above, the most recent and stringent constraints are from the analysis of [79], which rules out the presence of a turnover in the luminosity function brightward of $M_{\rm UV} \sim -15.5$. Actually, the data by [79] seem to suggest a possible flattening of the luminosity function for $M_{\rm UV} \gtrsim -15$, but the large errors and the systematic uncertainties due to the paucity of sources as well as incompleteness issues do not allow us to make robust conclusions; thus, in the following, we will not try to model the detailed shape of any possible bending and instead use the extrapolation of the steep Schechter fits the data by [78] with a sharp limit at $M_{\rm UV}^{\rm lim}$ [1].

The rationale is that at magnitudes fainter than $M_{\rm UV}^{\rm lim}$, the luminosity function flattens or even bends downward because the galaxy formation process becomes inefficient and/or because the power spectrum is cut off due to the microscopic nature of DM. Below we connect such a magnitude limit to two parameters describing these effects: a threshold halo mass $M_{\rm H}^{\rm GF}$ below which galaxy formation is hindered because of various processes, like photo-suppression by the intense UV background or inefficiency in atomic cooling by the low temperature and metallicity of small halos at high redshift (see [88–90]); an astroparticle property X specific of a given DM scenario (e.g., WDM mass), which characterizes the suppression of the power spectrum at small scales.

2.1. Halo Mass Function and Abundance Matching

We consider three common non-standard DM scenarios alternative to CDM: warm dark matter (WDM), fuzzy dark matter (ψDM), and self-interacting dark matter (SIDM). In all these scenarios, the number of small-mass halos is reduced relative to CDM; this is best specified in terms of the halo mass function, namely the number density of halos per comoving volume and halo mass $M_{\rm H}$ bins, which can be conveniently written in terms of the CDM one as

$$\frac{{\rm d}N}{{\rm d}M_{\rm H}\,{\rm d}V} = \frac{{\rm d}N_{\rm CDM}}{{\rm d}M_{\rm H}\,{\rm d}V}\left[1+\left(\frac{M_{\rm H}^{\rm cut}}{M_{\rm H}}\right)^{\beta}\right]^{-\gamma}, \tag{3}$$

where β and γ are shape parameters, and $M_{\rm H}^{\rm cut}$ is a cutoff halo mass. We calculate the CDM halo mass function by exploiting the Python `COLOSSUS` package [91] and the fitting formula by [92] for virial masses. The parameters (β, γ) in Equation (3) are instead derived from fits to the outcomes of numerical simulations in the considered DM scenarios; the related values of the parameters and the literature works from which these are taken ([36,38,39]), are reported in Table 1. We stress that to derive robust constraints on different DM scenarios based on the halo mass function, it is extremely important to rely on the results from detailed simulations (as done here) and not on semi-analytic derivations based on the excursion set formalism, whose outcomes on the shape of the mass function for masses $M_{\rm H} \lesssim M_{\rm H}^{\rm cut}$ are rather sensitive to several assumptions (e.g., the filter function used in deriving the mass variance from the power spectrum, the mass-dependence in the collapsing barrier, etc.; see [55,93,94]).

Table 1. Parameters describing the ratio of the halo mass function for different DM scenarios relative to the standard CDM in terms of the expression $[1+(M_{\rm H}^{\rm cut}/M_{\rm H})^{\beta}]^{-\gamma}$, where $M_{\rm H}$ is the halo mass and $M_{\rm H}^{\rm cut}$ is a characteristic cutoff scale; see Section 2.1 for details. The values of the parameters (β, γ), extracted from the fits to the outcomes of numerical simulations in the considered DM scenarios, are taken from the literature studies referenced in the last column.

Scenario	β	γ	Ref.
WDM	1.0	1.16	[36]
ψDM	1.1	2.2	[38]
SIDM	1.0	1.34	[39]

As to the cutoff mass $M_{\rm H}^{\rm cut}$, in WDM it is determined by free-streaming effects [36] and reads $M_{\rm H}^{\rm cut} \approx 1.9\times10^{10}\ {\rm M}_\odot\,(m_X/{\rm keV})^{-3.33}$ in terms of the particle mass m_X. However, note that this cutoff (often referred to as half-mode) mass is substantially larger by factors of a few 10^3 than the free streaming mass, i.e., the mass related to the typical length scale for the diffusion of WDM particles out of primordial perturbations. In ψDM, $M_{\rm H}^{\rm cut} \approx 1.6\times10^{10}$ ${\rm M}_\odot\ (m_X/10^{-22}\,{\rm eV})^{-1.33}$ is related to the coherent behavior of the particles [38] with mass m_X. In the SIDM scenario, $M_{\rm H}^{\rm cut} \approx 7\times10^{7}\ {\rm M}_\odot\,(T_X/{\rm keV})^{-3}$ can be linked to the visible sector temperature T_X when kinetic decoupling of the DM particles takes place [39].

In Figure 2, we illustrate the halo mass functions in the different DM scenarios at a reference redshift $z \approx 10$, to highlight the dependence on the particle property. For example, focusing on WDM, it is seen that the halo mass function progressively flattens with respect to that in standard CDM (black line); the deviation occurs at smaller halo masses for higher WDM particle masses m_X, so that the CDM behavior is recovered for $m_X \to \infty$. In the other DM scenarios, the behavior is similar, but the shape of the mass function past the low-mass end flattening can be appreciably different; for example, in the ψDM scenario, the mass function is strongly suppressed for small masses and actually bends downward rather than flattening, implying a strong reduction or even the absence of low mass halos.

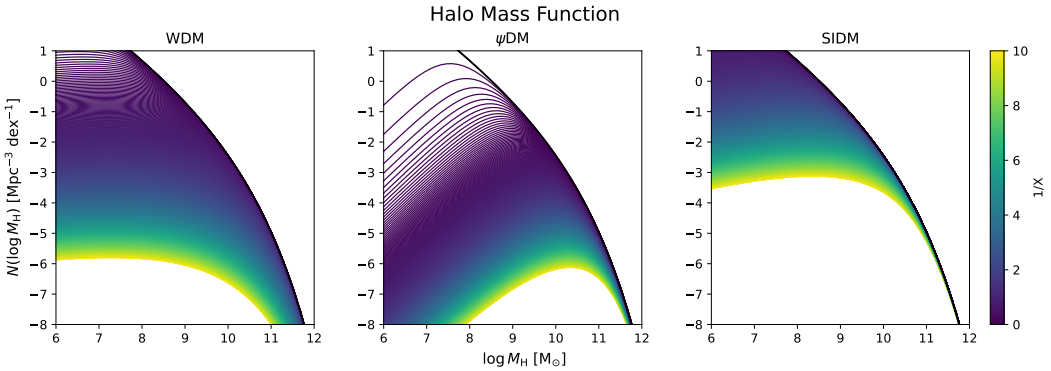

Figure 2. Halo mass function at a reference redshift $z \approx 10$ in different DM scenarios: WDM (left panel), ψDM (middle panel) and SIDM (right panel). The colorbar refers to values of keV$/m_X$ for WDM, 10^{-22} eV$/m_X$ for ψDM and keV$/T_X$ for SIDM. In all panels, the black line refers to the standard CDM scenario.

We now look for a relationship between UV magnitude and halo masses via the standard abundance matching technique [95–98], i.e., matching the cumulative number densities in galaxies and halos according to the expression

$$\int_{M_{\rm H}}^{+\infty} {\rm d}M'_{\rm H}\, \frac{{\rm d}N}{{\rm d}M'_{\rm H}\,{\rm d}V}(M'_{\rm H}, z|X) = \int_{-\infty}^{M_{\rm UV}} {\rm d}M'_{\rm UV}\, \frac{{\rm d}N}{{\rm d}M'_{\rm UV}\,{\rm d}V}(M'_{\rm UV}, z) \tag{4}$$

which implicitly defines a one-to-one monotonic relationship $M_{\rm UV}(M_{\rm H}, z|X)$; here, the quantity X stands for the specific property of the DM scenario that determines the behavior of the mass function for $M_{\rm H} \lesssim M_{\rm H}^{\rm cut}$: particle mass m_X in keV for WDM and in 10^{-22} eV for ψDM, and kinetic temperature $T_{\rm X}$ in keV for SIDM. In Figure 3, we show the outcome of this procedure in a reference redshift $z \approx 10$ in the different DM scenarios, highlighting its dependence on the particle property. Focusing on WDM as a representative case, it is seen that the $M_{\rm UV}(M_{\rm H}, z|m_x)$ relation progressively flattens toward small $M_{\rm H}$with respect to the standard CDM case, and especially so for smaller m_X; at the other end, the relation becomes indistinguishable from that in CDM for particle masses $m_X \gtrsim$ some keVs. At a given particle mass, the relation $M_{\rm H}(M_{\rm UV}, z|m_X)$ barely depends on redshift $z \gtrsim 6$, because the cosmic evolution of the UV luminosity function and the halo mass function mirror each other (see discussion by [78]). In the other DM scenarios, the behavior of the $M_{\rm UV}(M_{\rm H}, z|X)$ relation is similar but its shape for small halo masses is appreciably different; e.g., in the ψDM scenario, the relation flatten abruptly, reflecting the paucity of small halos in the mass function (see Figure 2).

The rationale is now to compute the cosmic SFR density $\rho_{\rm SFR}(z)$ according to Equation (2) by integrating the luminosity function down to a magnitude limit $M_{\rm UV}^{\rm lim}(M_{\rm H}^{\rm GF}, z|X)$ that depends on two parameters, namely the minimum halo mass for galaxy formation $M_{\rm H}^{\rm GF}$ and the astroparticle properties X of a given DM scenario, and hence to estimate these quantities by comparing $\rho_{\rm SFR}(z)$ with the observational determinations.

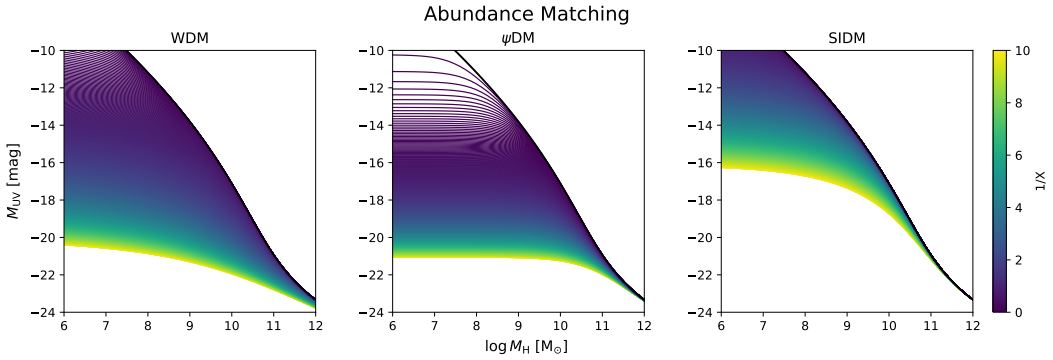

Figure 3. Relationship between the UV magnitude $M_{\rm UV}$ and the halo mass $M_{\rm H}$ at a reference redshift $z \approx 10$, derived from the abundance matching of the observed UV luminosity function and the halo mass function (see text for details) in different DM scenarios: WDM (left panel), ψDM (middle panel) and SIDM (right panel). The colorbar refers to values of keV$/m_X$ for WDM, 10^{-22} eV$/m_X$ for ψDM and keV$/T_X$ for SIDM. In all panels, the black line refers to the standard CDM scenario.

2.2. Bayesian Analysis

The descriptions provided in the previous sections highlight that the limiting UV magnitude $M_{\rm UV}^{\rm lim}$ depends on two parameters: the limiting halo mass for galaxy formation $M_{\rm H}^{\rm GF}$, and a quantity X specific to the DM scenario, that represent the particle mass m_X in units of keV for WDM, the particle mass m_X in units of 10^{-22} eV for ψDM, and the temperature of kinetic decoupling T_X in units of keV for SIDM. These two parameters are meant to effectively encompass a variety of effects that determine $M_{\rm UV}^{\rm lim}$, related to the efficiency of the galaxy formation process in small halos, and to the suppression in the number of low-mass halos due to the microscopic nature of DM. An added value of the empirical approach pursued here, which relies on extrapolation of the observed UV luminosity functions down to $M_{\rm UV}^{\rm lim}$, is that no further parameter is needed to predict the cosmic SFR density (besides the underlying assumption of an IMF, which in any case marginally affects the astroparticle constraints, as shown by [58]).

To estimate the two aforementioned parameters, we adopt a Bayesian MCMC framework, numerically implemented via the Python package `emcee` [99]. Since for large values of X, all the outcomes of the nonstandard scenario converge toward CDM, it is convenient to look for an estimate of $1/X$ instead of X to have a fitting parameter varying in a compact domain. We use a standard Gaussian likelihood $\mathcal{L}(\theta) \equiv -\sum_i \chi_i^2(\theta)/2$ where $\theta = \{M_{\rm H}^{\rm GF}, 1/X\}$ is the vector of parameters, and the summation is over different datasets; for the latter, the corresponding $\chi_i^2 = \sum_j [\mathcal{M}(z_j,\theta) - \mathcal{D}(z_j)]^2/\sigma_{\mathcal{D}}^2(z_j)$ is obtained by comparing our empirical model expectations $\mathcal{M}(z_j,\theta)$ to the data $\mathcal{D}(z_j)$ with their uncertainties $\sigma_{\mathcal{D}}^2(z_j)$, summing over the different redshifts z_j of the datapoints. Specifically, our overall data sample is constituted by robust measurements of the cosmic SFR density (see summary in Table 2) from the HST UV luminosity function data from HST [79], UV luminosity function early data from JWST [80], GRB counts data from Fermi [100], and (sub)mm luminosity function data from ALMA [101]. In the computation of the cosmic SFR density, we take into account the minimum observational magnitude limit $M_{\rm UV}^{\rm obs}$ of the different datasets.

We adopt flat priors $\pi(\theta)$ on the parameters within the ranges $\log M_{\rm H}^{\rm GF}[M_\odot] \in [6, 11]$, and $1/X \in [0, 10]$. We then sample the posterior distribution $\mathcal{P}(\theta) \propto \mathcal{L}(\theta)\,\pi(\theta)$ by running `emcee` with 10^4 steps and 200 walkers; each walker is initialized with a random position uniformly sampled from the (flat) priors. After checking the auto-correlation time, we remove the first 20% of the flattened chain to ensure burn-in; the typical acceptance fractions of the various runs are in the range of 30–40%.

Table 2. Overview of the estimate for the cosmic SFR density considered in the Bayesian analysis of this work. Values and uncertainties refer to log SFR $[M_\odot\ \mathrm{yr}^{-1}]$.

Data	Redshifts	Values	Uncertainties	Reference
UV LF [HST]	$\{3.8, 4.9, 5.9, 6.8, 7.9, 8.9, 10.4\}$	$\{-1.14, -1.4, -1.66, -1.85, -2.05, -2.61, -3.13\}$	$\{0.08, 0.07, 0.05, 0.06, 0.11, 0.11, 0.35\}$	[77–79]
UV LF [JWST]	$\{\sim 9, \sim 12, \sim 17\}$	$\{-2.90, -3.61, \lesssim -3.94\}$	$\{0.17, 0.27, 0.31\}$	[80]
GRB counts [Fermi]	$\{4.49, 5.49, 6.49, 7.74\}$	$\{-1.138, -1.423, -1.262, -1.508\}$	$\{0.184, 0.289, 0.359, 0.517\}$	[100]
(sub)mm LF [ALMA]	$\{4.00, 5.25\}$	$\{-1.218, -1.252\}$	$\{0.219, 0.612\}$	[101]

3. Results and Discussion

As a preliminary step, we analyze the data in the standard CDM scenario. The result is shown by the gray contours/lines in Figures 4–6. By construction, in the CDM model, the UV limiting magnitude $M_{\rm UV}^{\rm lim}$ depends only on the threshold minimum halo mass for galaxy formation. The marginalized constraint on the latter is found to be $\log M_{\rm H}^{GF}[M_\odot] \approx 9.4^{+0.2\,(+0.4)}_{-0.1\,(-0.4)}$, a value which is reasonably close to the photo-suppression mass expected by the intense UV background during reionization (e.g., [88]). The corresponding limiting magnitude at $z\sim10$ is around $M_{\rm UV}^{\rm lim} \approx -14.7$.

In the other DM scenarios, the situation is different because the limiting UV magnitude can also depend on the DM astroparticle property X. The results for WDM are illustrated by the red lines/contours in Figure 4. It is seen that there is a clear degeneracy between the WDM mass m_X and the threshold halo mass $M_{\rm H}^{\rm GF}$ for galaxy formation, in that the same value of the limiting UV magnitude $M_{\rm UV}^{\rm lim}$ can be obtained with smaller $M_{\rm H}^{\rm GF}$ and smaller m_X (see Figure 3). This is because lowering $M_{\rm H}^{\rm GF}$ extends the halo mass function toward smaller masses and, thus, allows more halos to be available for hosting galaxies while decreasing m_X progressively flattens the shape of the halo mass function, thus, reducing the number of halos and offsetting the previous effect. Such a situation is possible if m_X is not too low; otherwise, the reduction in the number of halos is so drastic that it cannot be compensated by reasonable values of $M_{\rm H}^{\rm GF}$; note the minimally acceptable $M_{\rm H}^{\rm GF}$ could be around $10^{7-8}\,M_\odot$, because below these masses atomic cooling becomes inefficient; a hard limit is set by minihalos of $10^6\,M_\odot$ where the first (pop-III) stars are thought to form.

The marginalized constraints for WDM turns out to be $\log M_{\rm H}^{GF}[M_\odot] \approx 7.6^{+2.2\,(+2.3)}_{-0.9\,(-3.3)}$ and $m_X \approx 1.2^{+0.3\,(11.3)}_{-0.4\,(-0.5)}$ keV, corresponding to a UV limiting magnitude $M_{\rm UV}^{\rm lim} \approx -13.3$. There is a clear peak in the posterior for the WDM mass around the keV scale, which is interesting because such a value has often been invoked to solve small-scale issues of CDM, like the missing satellite problems and the cusp-core controversy. However, larger values of $m_X \gtrsim$ a few keVs, that produce outcomes practically indistinguishable for CDM, are still well allowed (within 2σ) by the current estimates of the cosmic SFR density.

The situation for ψDM and SIDM is somewhat similar to that of WDM. The main difference resides in the behavior of the halo mass function at small masses, which induces a different shape in the relationship between $M_{\rm H}$ and $M_{\rm UV}$, and in turn, this affects the marginalized contraints . In the ψDM case, whose results are illustrated in Figure 5, only an upper limit of the threshold halo mass for galaxy formation $\log M_{\rm H}^{GF}[M_\odot] < 7.9\ (< 9.3)$ can be provided; however, the particle mass is constrained to $m_X \approx 3.7^{+1.8\,(+12.9.3)}_{-0.4\,(-0.5)} \times 10^{-22}$ eV, corresponding to a UV-limiting magnitude $M_{\rm UV}^{\rm lim} \approx -14.6$ at $z\sim10$. In the SIDM scenario, whose results are illustrated in Figure 5, the marginalized constraints read $\log M_{\rm H}^{GF}[M_\odot] \approx 7.6^{+2.2\,(+2.3)}_{-1.1\,(-3.2)}$ and $T_X \approx 0.21^{+0.04\,(+1.8)}_{-0.06\,(-0.07)}$ keV, corresponding to a UV limiting magnitude $M_{\rm UV}^{\rm lim} \approx -13.7$ at $z\sim10$. The overall marginalized constraints are summarized in Table 3.

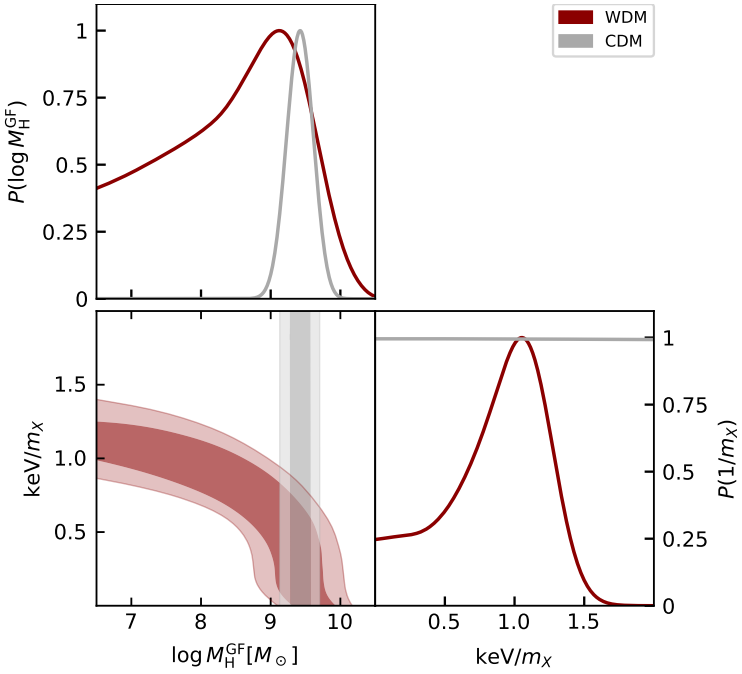

Figure 4. MCMC posterior distributions in the WDM scenario (red contours/lines), for the threshold halo mass for galaxy formation $M_{\rm H}^{\rm GF}$, and the inverse of the DM particle's mass keV/m_X. For reference, the outcomes in the standard CDM scenario are also reported (grey contours/lines). The contours show 68% and 95% confidence intervals, and the marginalized distributions are in arbitrary units (normalized to 1 at their maximum value).

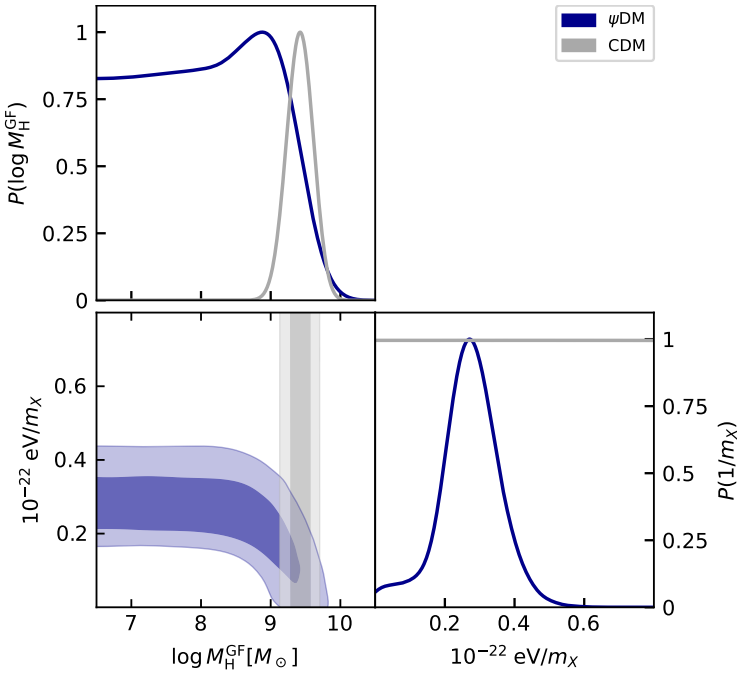

Figure 5. MCMC posterior distributions in the ψDM scenario (blue contours/lines), for the threshold halo mass for galaxy formation $M_{\rm H}^{\rm GF}$, and the inverse of the DM particle's mass 10^{-22} eV/m_X. For reference, the outcomes in the standard CDM scenario are also reported (grey contours/lines). The contours show 68% and 95% confidence intervals, and the marginalized distributions are in arbitrary units (normalized to 1 at their maximum value).

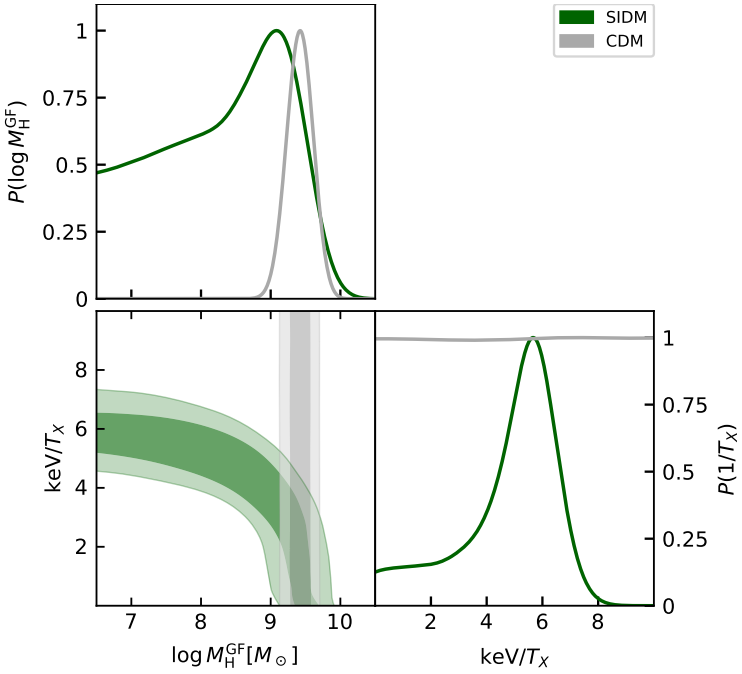

Figure 6. MCMC posterior distributions in the SIDM scenario (green contours/lines), for the threshold halo mass for galaxy formation $M_{\rm H}^{\rm GF}$, and the inverse of the DM kinetic temperature at decoupling keV/T_X. For reference, the outcomes in the standard CDM scenario are also reported (grey contours/lines). The contours show 68% and 95% confidence intervals, and the marginalized distributions are in arbitrary units (normalized to 1 at their maximum value).

Table 3. Marginalized posterior estimates (mean, 68% and 95% confidence limits are reported) of the parameters of the MCMC analysis for the different DM scenarios considered in the main text (WDM, ψDM and SIDM). Specifically, $M_{\rm H}^{\rm GF}$ is the threshold halo mass for galaxy formation, while the astroparticle quantity X in the third column represents the particle mass m_X in keV for WDM, the particle mass m_X in 10^{-22} eV for ψDM, and kinetic temperature T_X in keV for SIDM; The last two columns refer to the value of the Bayes information criterion (BIC) and the Deviance information criterium (DIC) for model comparison; see Section 3. The top half of the Table refers to the current constraints on the cosmic SFR density, while the bottom half to the forecasts for JWST observations extended down to UV magnitude $M_{\rm UV} \approx -13$, see Section 3.1 for details.

Scenario	$M_{\rm H}^{\rm GF}$	X	BIC	DIC
CDM	$9.4^{+0.2\,(+0.4)}_{-0.1\,(-0.4)}$	–	≈ 31	≈ 13
WDM	$7.6^{+2.2\,(+2.3)}_{-0.9\,(-3.3)}$	$1.2^{+0.3\,(+11.3)}_{-0.4\,(-0.5)}$	≈ 33	≈ 14
ψDM	$< 7.9\,(< 9.3)$	$3.7^{+1.8\,(+12.9)}_{-0.9\,(-1.4)}$	≈ 33	≈ 14
SIDM	$7.6^{+2.2\,(+2.3)}_{-1.1\,(-3.2)}$	$0.21^{+0.04\,(+1.8)}_{-0.06\,(-0.07)}$	≈ 33	≈ 14
CDM + JWST forecast	$< 7.2\,(< 8.5)$	–	≈ 89	≈ 130
WDM + JWST forecast	$< 6.6\,(< 8.2)$	$> 1.8\,(> 1.2)$	≈ 87	≈ 125
ψDM + JWST forecast	$6.2^{+1.3}_{-1.3}\,(< 8.2)$	$> 17.3\,(> 12)$	≈ 92	≈ 135
SIDM + JWST forecast	$< 6.8\,(< 8.3)$	$> 0.4\,(> 0.3)$	≈ 89	≈ 130

In Figure 7, we illustrate the performance of our best fits on the observed cosmic SFR density; all DM scenarios (colored lines) reproduce comparably well with the available data. This is also highlighted by the 95% credible interval from sampling the posterior distribution, which is shown only in the WDM case for clarity (red-shaded area). In terms of projection on this observable, different DM scenarios are consistent with each other, approximately within 2σ.

We can also attempt a quantitative model comparison analysis using the Bayes information criterion [102,103], which is defined as BIC$\equiv -2\ln\mathcal{L}_{\rm max} + N_{\rm par}\ln N_{\rm data}$ in terms of the maximum likelihood estimate $\mathcal{L}_{\rm max}$, of the number of parameters $N_{\rm par}$, and the number of data points $N_{\rm data}$; the BIC comes from approximating the Bayes factor, which gives the posterior odds of one model against another, presuming that the models are equally favored a priori. Another possibility, which may be less sensitive to priors, is the Deviance information criterion [104], which is defined as DIC$\equiv -2\log\mathcal{L}(\bar{\theta}) + 2\,p_D$ where the overbar denotes the mean and the effective number of parameters p_D is estimated as $p_D \approx -2\overline{\log\mathcal{L}(\theta)} - 2\log\mathcal{L}(\bar{\theta})$. Note that what matters is only the relative value of the BIC or DIC between different models; in particular, a difference larger than 10 indicates robust evidence in favor of the model with the smaller value. The values of the BIC and the DIC (for the different DM scenarios) are reported in Table 3, and do not suggest clear evidence in favor of one scenario over the others or over the standard CDM.

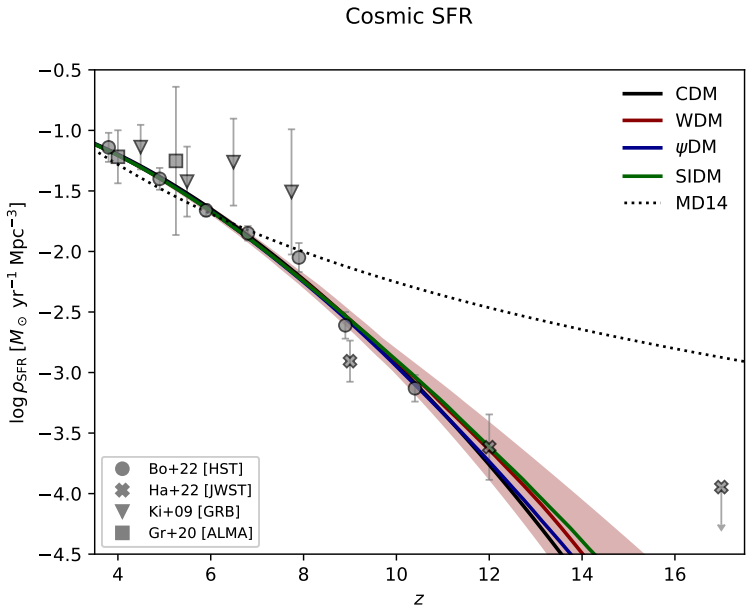

Figure 7. The cosmic SFR density as a function of redshift. Data are from UV-HST (circles; [77,78]), UV-JWST (crosses; [80]), GRB-Fermi (inverse triangles; [100]), and (sub)mm-ALMA (squares; [101]). Lines illustrate the best fits from the MCMC analysis in various DM scenarios: CDM (black), WDM (red), ψDM (blue), and SIDM (green). The typical 2σ credible interval from the sampling of the posterior distribution is shown, for clarity, only in the WDM scenario, as a red shaded area. For reference, the dotted line is the classic fitting formula gauged at $z \lesssim 6$ by [85].

3.1. Forecasts for JWST

As mentioned in Section 2 and shown in Figure 1, the early data from JWST at $z\sim12$ seems to indicate a slowing of the evolution of the UV luminosity function with respect to the lower $z \lesssim 10$. The effect is also evident on the cosmic SFR density in Figure 7, since the JWST data (crosses) at $z\sim9$–12 are around the same value as the HST ones (circles), but the former refers to a UV luminosity function integrated to $M_{\rm UV}^{\rm obs} \approx -17$ while the latter refers to $M_{\rm UV}^{\rm obs} \approx -13$.

Aside from the possible issues related to systematics and completeness effects in the early JWST observations that will hopefully be cleared by future campaigns, one can ask the question: what if the JWST data are confirmed and extended to ultra-faint magnitudes? To make a sound and conservative forecast of such a circumstance on the astroparticle constraints of this work, we proceed as follows. We scaled up by 0.4 dex the current SFR density estimate from JWST by [80] at $z \gtrsim 9$, to reflect the same increase in $\rho_{\rm SFR}$ of the HST data by [79] when integrating the luminosity function from $M_{\rm UV}^{\rm obs} \approx -17$ to $M_{\rm UV}^{\rm obs} \approx -13$;

we also assign a relative uncertainty to the JWST data comparable to that of the HST one by [79].

In Figure 8, we illustrate the marginalized posteriors on the astroparticle quantities in the WDM, ψDM, and SIDM scenarios. Plainly, the appreciably higher values of the cosmic SFR density implied from the putative JWST data tend to go in tension with the suppression of the power spectrum at a small scale in the non-CDM scenarios, erasing the bell-shaped posterior still allowed by the current data. As a consequence, rather stringent lower limits on the astroparticle quantities can be derived: WDM mass $m_X \gtrsim 1.8\,(1.2)$ keV, ψDM mass $m_X \gtrsim 17.3\,(12) \times 10^{-22}$ eV, and SIDM kinetic temperature $T_X > 0.4\,(0.3)$ keV. These lower bounds would be competitive with current literature constraints that tend to exclude part of the parameter space in non-CDM models (see references in Section 1). Yet, the independent and basic nature of the cosmic SFR density observable may provide constraints less affected by systematics and model-dependent interpretations.

Finally, a note in Table 3 states that fitting to the forecasted JWST data will require a quite low galaxy formation threshold $M_{\rm H}^{\rm GF}$ in CDM (and even more extreme values in the other scenarios); nonetheless, the upper bounds at 2σ are still consistent with the atomic cooling limit, so the forecasted JWST data should not present an insurmountable astrophysical challenge for CDM.

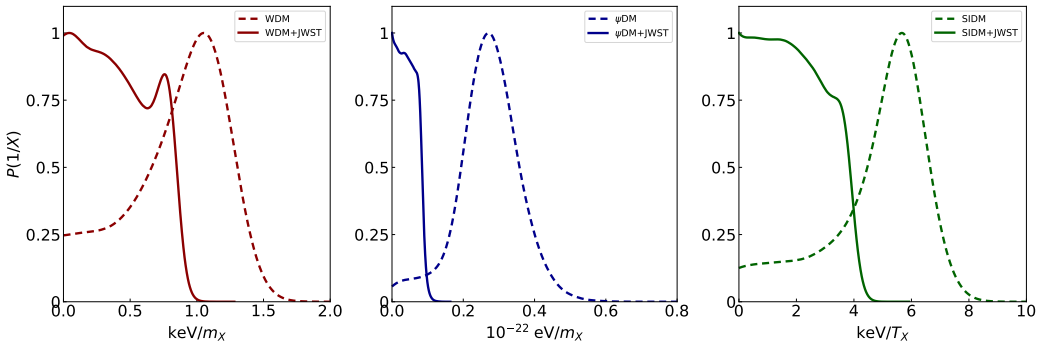

Figure 8. Forecasts of marginalized posteriors on the WDM mass (left panel), ψDM mass (middle panel), and SIDM kinetic temperature at decoupling (right panel) based on prospective data at $z \gtrsim 10$ from JWST (solid lines; see text for details). For reference, the dashed lines illustrate the current constraints from Figures 4–6. The marginalized distributions are in arbitrary units (normalized to 1 at their maximum value).

4. Summary

In this work, we have derived astroparticle constraints for different dark matter scenarios alternative to standard cold dark matter (CDM), namely warm dark matter (WDM), fuzzy dark matter (ψDM), and self-interacting dark matter (SIDM), from recent determination of the cosmic star formation rate (SFR) density at high redshifts $z \gtrsim 4$. We have relied on the UV luminosity functions measured from blank field surveys by the Hubble Space Telescope up to $z \lesssim 10$ and UV magnitudes $M_{\rm UV} \lesssim -17$. We have extrapolated these to fainter, yet unexplored magnitudes and performed abundance matching with the halo mass functions in a given DM scenario, thus, obtaining a redshift-dependent relationship between the UV magnitude and the halo mass.

Then, we have computed the cosmic SFR density by integrating the extrapolated UV luminosity function down to a faint magnitude limit $M_{\rm UV}^{\rm lim}$, which is determined by the abundance matching relationship by the minimum threshold halo mass $M_{\rm H}^{\rm GF}$ for galaxy formation, and by the astroparticle quantity X specific to each DM scenario (e.g., WDM particle mass).

Finally, we have performed Bayesian inference on the two parameters $M_{\rm H}^{\rm GF}$ and X via a standard MCMC technique by comparing the cosmic SFR density of our approach with current observational estimates at $z \gtrsim 4$, thus, deriving definite astroparticle constraints:

a WDM particle mass $m_X \approx 1.2^{+0.3\,(11.3)}_{-0.4\,(-0.5)}$ keV, a ψDM particle mass $m_X \approx 3.7^{+1.8\,(+12.9)}_{-0.4\,(-0.5)} \times 10^{-22}$ eV, and a SIDM temperature at kinetic decoupling $T_X \approx 0.21^{+0.04\,(+1.8)}_{-0.06\,(-0.07)}$ keV at 68% (95%) confidence level.

In addition, from the same analysis, we have estimated that for CDM, the minimum halo mass for galaxy formation is well constrained to $\log M_{\rm H}^{\rm GF}[M_\odot] \approx 9.4^{+0.2\,(+0.4)}_{-0.9\,(-0.4)}$, which is pleasingly close to the photo-suppression mass expected at high redshifts due to the intense UV background. On the other hand, for non-CDM scenarios, we have estimated a smaller $M_{\rm H}^{\rm GF} \lesssim 10^8\,M_\odot$, which is a value closer to the atomic cooling limit, although yet poorly constrained due to the degeneracy with the astroparticle property.

In a future perspective, we have forecasted how such constraints will be strengthened if the early data on the UV luminosity function at $z \gtrsim 10$ from the James Webb Space Telescope (JWST) will be confirmed and extended to ultra-faint magnitudes; these would imply upper limits on the WDM mass $m_X \gtrsim 1.8\,(\gtrsim 1.2)$ keV, on the ψDM mass of $m_X \gtrsim 17.3\,(\gtrsim 12) \times 10^{-22}$ eV, and on the SIDM kinetic temperature $T_X \gtrsim 0.4\,(\gtrsim 0.3)$ keV, which are competitive yet independent with respect to current literature constraints from a variety of other probes.

Our analysis highlights the relevance of upcoming ultra-faint galaxy surveys in the (pre)reionization era via JWST (see [105–107]) as a direct probe both of the astrophysics of galaxy formation at small scales, and of the microscopic nature of the elusive dark matter particles.

Author Contributions: All authors have equally contributed to design, to perform the analysis and to the writing of this paper. All authors have read and agreed to the published version of the manuscript.

Funding: We thank the three anonymous referees for their useful comments and suggestions. A.L. acknowledges funding from the EU H2020-MSCA-ITN-2019 project 860744 *BiD4BESt: Big Data applications for black hole Evolution STudies* and from the PRIN MIUR 2017 prot. 20173ML3WW, *Opening the ALMA window on the cosmic evolution of gas, stars, and supermassive black holes*.

Institutional Review Board Statement: Not applicable.

Informed Consent Statement: Not applicable.

Acknowledgments: We thank L. Boco, C. Baccigalupi, and P. Salucci for stimulating discussions.

Conflicts of Interest: The authors declare no conflict of interest.

Note

[1] In fact, one can easily adopt a smooth bending of the luminosity function and set instead the upper limit of integration in Equation (2) just to $M_{\rm UV}^{\rm obs}$. For example, [79] empirically suggest to multiply Equation (1) by a factor $10^{0.4\,(\alpha+1)/2\times(M_{\rm UV}+16)^2/(M_{\rm UV}^{\rm lim}+16)}$ for $M_{\rm UV} \gtrsim -16$. We have checked that in the computation of the cosmic SFR, this produces practically indistinguishable results with respect to our simple treatment.

References

1. Meurer, G.R.; Heckman, T.M.; Calzetti, D. Shedding Light on Dark Matter at Colliders. *Int. J. Mod. Phys.* **2013**, *28*, 1330052.
2. Kahlhoefer, F. Review of LHC dark matter searches.*Int. J. Mod. Phys.* **2017**, *32*, 1730006. [CrossRef]
3. Argyropoulos, S.; Brandt, O.; Haisch, U. Collider Searches for Dark Matter through the Higgs Lens. *Symmetry* **2021**, *13*, 2406. [CrossRef]
4. Aprile, E. et al. [XENON Collaboration]. Dark Matter Search Results from a One Ton-Year Exposure of xenon1t. *Phys. Rev. Lett.* **2018**, *121*, 111302. [CrossRef] [PubMed]
5. Bernabei, R.; Belli, P.; Caracciolo, V.; Cerulli, R.; Merlo, V.; Cappella, F.; D'Angelo, A.; Incicchitti, A.; di Marco, A.; Dai, C.J.; et al. DAMA/LIBRA-phase2 results and implications on several dark matter scenarios. *Int. J. Mod. Phys.* **2020**, *35*, 2044023. [CrossRef]
6. Ackermann, M. et al. [The Fermi LAT Collaboration]. Limits on dark matter annihilation signals from the Fermi LAT 4-year measurements of the isotropic gamma-ray background. *J. Cosmol. Astropart. Phys.* **2015**, *2015*, 8. [CrossRef]
7. Ackermann, M. et al. [The Fermi LAT Collaboration]. The Fermi Galactic Center GeV Excess and Implications for Dark Matter. *Astrophys. J.* **2017**, *840*, 43. [CrossRef]
8. Albert, A. et al. [The Fermi-LAT and DES Collaborations]. Searching for Dark Matter Annihilation in Recently Discovered Milky Way Satellites with Fermi-LAT. *Astrophys. J.* **2017**, *834*, 110. [CrossRef]

9. Zornoza, J. Review on Indirect Dark Matter Searches with Neutrino Telescopes. *Universe* **2021**, *7*, 415. [CrossRef]
10. Bertone, G.; Hooper, D. History of dark matter. *Rev. Mod. Phys.* **2018**, *90*, 045002. [CrossRef]
11. Frenk, C.S.; White, S.D.M. Dark matter and cosmic structure. *Ann. Phys.* **2012**, *524*, 507–534. [CrossRef]
12. Lapi, A..; Danese, L. A Stochastic Theory of the Hierarchical Clustering. I. Halo Mass Function. *Astrophys. J.* **2020**, *903*, 117. [CrossRef]
13. Aghanim, M. et al. [Planck Collaboration]. Planck 2018 results. VI. Cosmological parameters. *Astron. Astrophys.* **2020**, *641*, A6. [CrossRef]
14. Navarro, J.F.; Frenk, C.S.; White, S.D.M. A Universal Density Profile from Hierarchical Clustering. *Astrophys. J.* **1997**, *490*, 493. [CrossRef]
15. de Blok, W.J.G.; Walter, F.; Brinks, E.; Trachternach, C.; Oh, S.-H.; Kennicutt, R.C.Jr. High-Resolution Rotation Curves and Galaxy Mass Models from THINGS. *Astron. J.* **2008**, *136*, 2648. [CrossRef]
16. Boylan-Kolchin, M.; Bullock, J.S.; Kaplinghat, M. The Milky Way's bright satellites as an apparent failure of LambdaCDM. *Mon. Not. R. Astron. Soc.* **2012**, *422*, 1203–1218. [CrossRef]
17. Bullock, J.S.; Boylan-Kolchin, M. Small-Scale Challenges to the ΛCDM Paradigm. *Annu. Rev. Astron. Astrophys.* **2017**, *55*, 343–387. [CrossRef]
18. Gentile, G.; Famaey, B.; Zhao, H.; Salucci, P. Universality of galactic surface densities within one dark halo scale-length. *Nature* **2009**, *461*, 627–628. [CrossRef]
19. McGaugh, S.S.; Lelli, F.; Schombert, J.M. Radial Acceleration Relation in Rotationally Supported Galaxies. *Phys. Rev. Lett.* **2016**, *117*, 201101. [CrossRef]
20. El-Zant, A.; Shlosman, I.; Hoffman, Y. Dark Halos: The flattening of the density cusp by dynamical friction. *Astrophys. J.* **2001**, *560*, 636. [CrossRef]
21. Tonini, C.; Lapi, A.; Salucci, P. Angular Momentum Transfer in Dark Matter Halos: Erasing the Cusp. *Astrophys. J.* **2006**, *649*, 591. [CrossRef]
22. Pontzen, A.; Governato, F. Cold dark matter heats up. *Nature* **2014**, *506*, 171–178. [CrossRef] [PubMed]
23. Peirani, S.; Dubois, Y.; Volonteri, M.; Devriendt, J.; Bundy, K.; Silk, J.; Pichon, C.; Kaviraj, S.; Gavazzi, R.; Habouzit, M. Density profile of dark matter haloes and galaxies in the HORIZON-AGN simulation: The impact of AGN feedback. *Mon. Not. R. Astron. Soc.* **2017**, *472*, 2153–2169. [CrossRef]
24. Freundlich, J.; Jiang, F.; Dekel, A.; Cornuault, N.; Ginzburg, O.; Koskas, R.; Lapiner, S.; Dutton, A.; Maccio, A.V. A model for core formation in dark matter haloes and ultra-diffuse galaxies by outflow episodes. *Mon. Not. R. Astron. Soc.* **2020**, *491*, 4523–4542. [CrossRef]
25. Bertone, G.; Hooper, D.; Silk, J. Particle dark matter: Evidence, candidates and constraints. *Phys. Rev.* **2004**, *405*, 279–390. [CrossRef]
26. Feng, J.L. Dark Matter Candidates from Particle Physics and Methods of Detection. *Annu. Rev. Astron. Astrophys.* **2010**, *48*, 495–545. [CrossRef]
27. Salucci, P.; Esposito, G.; Lambiase, G.; Battista, E.; Benetti, M.; Bini, D.; Boco, L.; Sharma, G.; Bozza, V.; Buoninfante, L.; et al. Einstein, Planck and Vera Rubin: Relevant encounters between the Cosmological and the Quantum Worlds. *Front. Phys.* **2021**, *8*, 603190. [CrossRef]
28. Kusenko, A. Sterile neutrinos: The dark side of the light fermions. *Phys. Rev.* **2009**, *481*, 1–28. [CrossRef]
29. Adhikari, R.; Agostini, M.; Ky, N.A.; Araki, T.; Archidiacono, M.; Bahr, M.; Baur, J.; Behrens, J.; Bezrukov, F.; Bhupal Dev, P.S.; et al. A White Paper on keV sterile neutrino Dark Matter. *J. Cosmol. Astropart. Phys.* **2017**, *1*, 25. [CrossRef]
30. Bode, P.; Ostriker, J.P.; Turok, N. Halo Formation in Warm Dark Matter Models. *Astrophys. J.* **2001**, *556*, 93. [CrossRef]
31. Lovell, M.R.; Frenk, C.S.; Eke, V.R.; Jenkins, A.; Gao, L.; Theuns, T. The properties of warm dark matter haloes. *Mon. Not. R. Astron. Soc.* **2014**, *439*, 300–317. [CrossRef]
32. Hu, W.; Barkana, R.; Gruzinov, A. Fuzzy Cold Dark Matter: The Wave Properties of Ultralight Particles. *Phys. Rev. Lett.* **2000**, *85*, 1158. [CrossRef] [PubMed]
33. Hui, L.; Ostriker, J.P.; Tremaine, S.; Witten, E. Ultralight scalars as cosmological dark matter. *Phys. Rev. D* **2017**, *95*, 043541. [CrossRef]
34. Vogelsberger, M.; Zavala, J.; Cyr-Racine, F.-Y.; Pfrommer, C.; Bringmann, T.; Sigurdson, K. ETHOS—An effective theory of structure formation: Dark matter physics as a possible explanation of the small-scale CDM problems. *Mon. Not. R. Astron. Soc.* **2016**, *460*, 1399–1416. [CrossRef]
35. Tulin, S.; Yu, H.-B. Dark Matter Self-interactions and Small Scale Structure. *Phys. Rep.* **2018**, *730*, 1–57. [CrossRef]
36. Schneider, A.; Smith, R.E.; Maccio, A.; Moore, B. Non-linear evolution of cosmological structures in warm dark matter models. *Mon. Not. R. Astron. Soc.* **2012**, *424*, 684–698. [CrossRef]
37. Dayal, P.; Mesinger, A.; Pacucci, F. Early Galaxy Formation in Warm Dark Matter Cosmologies. *Astrophys. J.* **2015**, *806*, 67. [CrossRef]
38. Schive, H.-Y.; Chiueh, T.; Broadhurst, T.; Huang, K.-W. Contrasting Galaxy Formation from Quantum Wave Dark Matter, ψDM, with ΛCDM, using Planck and Hubble Data. *Astrophys. J.* **2016**, *818*, 89. [CrossRef]
39. Huo, R.; Kaplinghat, M.; Pan, Z.; Yu, H.-B. Signatures of self-interacting dark matter in the matter power spectrum and the CMB. *Phys. Lett. B* **2018**, *783*, 76–81. [CrossRef]

40. Menci, N.; Grazian, A.; Lamastra, A.; Calura, F.; Castellano, M.; Santini, P. Galaxy Formation in Sterile Neutrino Dark Matter Models. *Astrophys. J.* **2018**, *854*, 1. [CrossRef]
41. Lovell, M.R. Toward a General Parameterization of the Warm Dark Matter Halo Mass Function. *Astrophys. J.* **2020**, *847*, 147. [CrossRef]
42. Romanello, M.; Menci, N.; Castellano, M. The Epoch of Reionization in Warm Dark Matter Scenarios. *Universe* **2021**, *7*, 365. [CrossRef]
43. Kulkarni, M.; Ostriker, J.P. What is the halo mass function in a fuzzy dark matter cosmology? *Mon. Not. R. Astron. Soc.* **2022**, *510*, 1425. [CrossRef]
44. Viel, M.; Becker, G.; Bolton, J.S.; Haehnelt, M.G. Warm dark matter as a solution to the small scale crisis: New constraints from high redshift Lyman-alpha forest data. *Phys. Rev.* **2013**, *88*, 043502. [CrossRef]
45. Irsic, V. New constraints on the free-streaming of warm dark matter from intermediate and small scale Lyman-α forest data. *Phys. Rev.* **2017**, *96*, 023522.
46. Irsic, V., First Constraints on Fuzzy Dark Matter from Lyman-α Forest Data and Hydrodynamical Simulations. *Phys. Rev. Lett.* **2017**, *119*, 031302. [CrossRef]
47. Villasenor, B.; Robertson, B.; Madau, P.; Schneider, E. New Constraints on Warm Dark Matter from the Lyman-α Forest Power Spectrum. *arXiv* **2022**, arXiv:2209.14220
48. Pacucci, F.; Mesinger, A.; Haiman, Z. Focusing on Warm Dark Matter with Lensed High-redshift Galaxies. *Mon. Not. R. Astron. Soc.* **2013**, *435*, L53. [CrossRef]
49. Menci, N.; Grazian, A.; Castellano, M.; Sanchez, N.G. A Stringent Limit on the Warm Dark Matter Particle Masses from the Abundance of $z = 6$ Galaxies in the Hubble Frontier Fields. *Astrophys. J.* **2016**, *825*, L1. [CrossRef]
50. Shirasaki, M.; Ishiyama, T.; Ando, S. Virial Halo Mass Function in the Planck Cosmology. *Astrophys. J.* **2021**, *922*, 89. [CrossRef]
51. Sabti, N.; Munoz, J.B.; Blas, D. New Roads to the Small-scale Universe: Measurements of the Clustering of Matter with the High-redshift UV Galaxy Luminosity Function. *Astrophys. J.* **2022**, *928*, L20. [CrossRef]
52. De Souza, R.S.; Mesinger, A.; Ferrara, A.; Haiman, Z.; Perna, R.; Yoshida, N. Constraints on Warm Dark Matter models from high-redshift long gamma-ray bursts. *Mon. Not. R. Astron. Soc.* **2012**, *432*, 3218–3227. [CrossRef]
53. Lapi, A.; Mancuso, C.; Celotti, A.; Danese, L. Galaxy Evolution at High Redshift: Obscured Star Formation, GRB Rates, Cosmic Reionization, and Missing Satellites. *Astrophys. J.* **2017**, *835*, 37. [CrossRef]
54. Barkana, R.; Haiman, Z.; Ostriker, J.P. Constraints on Warm Dark Matter from Cosmological Reionization. *Astrophys. J.* **2001**, *558*, 482. [CrossRef]
55. Lapi, A.; Danese, L. Cold or warm? Constraining dark matter with primeval galaxies and cosmic reionization after Planck. *J. Cosmol. Astropart. Phys.* **2015**, *2015*, 3. [CrossRef]
56. Dayal, P.; Choudhury, T.R.; Bromm, V.; Pacucci, F. Reionization and Galaxy Formation in Warm Dark Matter Cosmologies. *Astrophys. J.* **2017**, *836*, 16. [CrossRef]
57. Carucci, I.P.; Corasaniti, P. Cosmic Reionization History and Dark Matter Scenarios. *Phys. Rev. D* **2019**, *99*, 023518. [CrossRef]
58. Lapi, A.; Ronconi, T.; Boco, L.; Shankar, F.; Krachmalnicoff, N.; Baccigalupi, C.; Danese, L. Astroparticle Constraints from Cosmic Reionization and Primordial Galaxy Formation. *Universe* **2022**, *8*, 476. [CrossRef]
59. Vegetti, S.; Despali, G.; Lovell, M.R.; Enzi, W. Constraining sterile neutrino cosmologies with strong gravitational lensing observations at redshift $z{\sim}0.2$. *Mon. Not. R. Astron. Soc.* **2018**, *481*, 3661. [CrossRef]
60. Ritondale, E.; Vegetti, S.; Despali, G.; Auger, M.W.; Koopmans, L.V. E.; McKean, J.P. Low-mass halo perturbations in strong gravitational lenses at redshift $z{\sim}0.5$ are consistent with CDM. *Mon. Not. R. Astron. Soc.* **2018**, *485*, 2179. [CrossRef]
61. Carucci, I.P.; Villaescusa-Navarro, F.; Viel, M.; Lapi, A. Warm dark matter signatures on the 21cm power spectrum: Intensity mapping forecasts for SKA. *J. Cosmol. Astropart. Phys.* **2015**, *2015*, 047. [CrossRef]
62. Boyarsky, A.; Drewes, M.; Lasserre, T.; Mertens, S.; Ruchayskiy, O. Sterile neutrino Dark Matter. *Prog. Part. Nucl. Phys.* **2019**, *104*, 1–45. [CrossRef]
63. Chatterjee, A.; Dayal, P.; Choudhury, T.R.; Hutter, A. Ruling out 3 keV warm dark matter using 21 cm EDGES data. *Mon. Not. R. Astron. Soc.* **2019**, *487*, 3560–3567. [CrossRef]
64. Rudakovskyi, A.; Savchenko, D.; Tsizh, M. Can EDGES observation favour any dark matter model? *Mon. Not. R. Astron. Soc.* **2020**, *497*, 3393–3399. [CrossRef]
65. Bringmann, T.; Kahlhoefer, F.; Schmidt-Hoberg, K.; Walia, P. Strong Constraints on Self-Interacting Dark Matter with Light Mediators. *Phys. Rev. Lett.* **2017**, *118*, 141802. [CrossRef] [PubMed]
66. Grand, R.J.J.; White, S.D.M. Dark matter annihilation and the Galactic Centre Excess. *Mon. Not. R. Astron. Soc.* **2022**, *511*, L55. [CrossRef]
67. Weisz, D.R.; Johnson, B.D.; Conroy, C. The Very Faint End of the UV Luminosity Function over Cosmic Time: Constraints from the Local Group Fossil Record. *Astrophys. J.* **2014**, *794*, L3. [CrossRef]
68. Weisz, D.R.; Boylan-Kolchin, M. Local Group ultra-faint dwarf galaxies in the reionization era. *Mon. Not. R. Astron. Soc.* **2017**, *469*, L83–L88. [CrossRef]
69. Calabrese, E.; Spergel, D. Ultra-light dark matter in ultra-faint dwarf galaxies. *Mon. Not. R. Astron. Soc.* **2016**, *460*, 4397–4402. [CrossRef]
70. Burkert, A. Fuzzy Dark Matter and Dark Matter Halo Cores. *Astrophys. J.* **2020**, *904*, 161. [CrossRef]

71. Kennedy, R.; Frenk, C.; Cole, S.; Benson, A. Constraining the warm dark matter particle mass with Milky Way satellites. *Mon. Not. R. Astron. Soc.* **2014**, *442*, 2487–2495. [CrossRef]
72. Horiuchi, S.; Humphrey, P.J.; Onorbe, J.; Abazajian, K.N.; Kaplinghat, M.; Garrison-Kimmel, S. Sterile neutrino dark matter bounds from galaxies of the Local Group. *Phys. Rev. D* **2014**, *89*, 025017. [CrossRef]
73. Lovell, M.R.; Bose, S.; Boyarsky, A.; Cole, S.; Frenk, C.S.; Gonzalez-Perez, V.; Kennedy, R.; Ruchayskiy, O.; Smith, A. Satellite galaxies in semi-analytic models of galaxy formation with sterile neutrino dark matter. *Mon. Not. R. Astron. Soc.* **2016**, *461*, 60. [CrossRef]
74. Nadler, E.O.; Birrer, S.; Gilman, D.; Wechsler, R.H.; Du, X.; Benson, A.; Nierenberg, A.M.; Treu, T. Dark Matter Constraints from a Unified Analysis of Strong Gravitational Lenses and Milky Way Satellite Galaxies. *Astrophys. J.* **2021**, *917*, 7. [CrossRef]
75. Newton, O.; Leo, M.; Cautun, M.; Jenkins, A.; Frenk, C.S.; Lovell, M.R.; Helly, J.C.; Benson, A.J.; Cole, S. Constraints on the properties of warm dark matter using the satellite galaxies of the Milky Way. *J. Cosmol. Astropart. Phys.* **2021**, *8*, 62. [CrossRef]
76. Enzi, W.; Murgia, R.; Newton, O.; Vegetti, S.; Frenk, C.; Viel, M.; Cautun, M.; Fassnacht, C.D.; Auger, M.; Despali, G.; et al. Joint constraints on thermal relic dark matter from strong gravitational lensing, the Ly α forest, and Milky Way satellites. *Mon. Not. R. Astron. Soc.* **2021**, *506*, 5848. [CrossRef]
77. Oesch, P.A.; Bouwens, R.J.; Illingworth, G.D.; Labbé, I.; Stefanon, M. The Dearth of $z\sim10$ Galaxies in All HST Legacy Fields—The Rapid Evolution of the Galaxy Population in the First 500 Myr. *Astrophys. J.* **2018**, *855*, 105. [CrossRef]
78. Bouwens, R.J.; Oesch, P.A.; Stefanon, M.; Illingworth, G.; Labbé, I.; Reddy, N.; Atek, H.; Montes, M.; Naidu, R.; Nanayakkara, T.; et al. New Determinations of the UV Luminosity Functions from $z\sim9$ to 2 Show a Remarkable Consistency with Halo Growth and a Constant Star Formation Efficiency. *Astron. J.* **2021**, *162*, 47. [CrossRef]
79. Bouwens, R.J.; Illingworth, G.; Ellis, R.S.; Oesch, P.A.; Stefanon, M. $z\sim2-9$ galaxies magnified by the Hubble Frontier Field Clusters II: Luminosity functions and constraints on a faint end turnover. *arXiv* **2022**, arXiv:2205.11526.
80. Harikane, Y.; Ouchi, M.; Oguri, M.; Ono, Y.; Nakajima, K.; Isobe, Y.; Umeda, H.; Mawatari, K.; Zhang, Y. A Comprehensive Study on Galaxies at $z\sim9$–17 Found in the Early JWST Data: UV Luminosity Functions and Cosmic Star-Formation History at the Pre-Reionization Epocht. *arXiv* **2022**, arXiv:2208.01612.
81. Chabrier, G. Galactic Stellar and Substellar Initial Mass Function. *Publ. Astron. Soc. Pacific* **2003**, *115*, 763. [CrossRef]
82. Meurer, G.R.; Heckman, T.M.; Calzetti, D. Dust Absorption and the Ultraviolet Luminosity Density at $z\sim3$ as Calibrated by Local Starburst Galaxies. *Astrophys. J.* **1999**, *521*, 64. [CrossRef]
83. Bouwens, R.J.; Illingworth, G.D.; Oesch, P.A. UV-continuum slopes of >4000 $z\sim4-8$ galaxies from the HUDF/XDF, HUDF09, ERS, CANDELS-South, and CANDELS-North fields. *Astrophys. J.* **2014**, *793*, 115. [CrossRef]
84. Kennicutt, R.C.; Evans, N.J. Star Formation in the Milky Way and Nearby Galaxies. *Annu. Rev. Astron. Astrophys.* **2012**, *50*, 531–608. [CrossRef]
85. Madau, P.; Dickinson, M. Cosmic Star-Formation History. *Annu. Rev. Astron. Astrophys.* **2014**, *52*, 415. [CrossRef]
86. Cai, Z.; Lapi, A.; Bressan, A.; De Zotti, G.; Negrello, M.; Danese, L. A Physical Model for the Evolving Ultraviolet Luminosity Function of High Redshift Galaxies and their Contribution to the Cosmic Reionization. *Astrophys. J.* **2014**, *785*, 65 [CrossRef]
87. Robertson, B.E.; Ellis, R.S.; Furlanetto, S.R.; Dunlop, J.S. Cosmic reionization and early star-forming galaxies: A joint analysis of new constraints from *Planck* and *Hubble Space Telescope*. *Astrophys. J.* **2015**, *802*, L19. [CrossRef]
88. Finkelstein, S.L.; D'Aloisio, A.; Paardekooper, J.-P.; Ryan, R., Jr.; Behroozi, P.; Finlator, K.; Livermore, R.; Upton Sanderbeck, P.R.; Dalla Vecchia, C.; Khochfar, S. Conditions for Reionizing the Universe with a Low Galaxy Ionizing Photon Escape Fraction. *Astrophys. J.* **2019**, *879*, 36. [CrossRef]
89. Efstathiou, G. Suppressing the formation of dwarf galaxies via photoionization. *Mon. Not. R. Astron. Soc.* **1992**, *256*, 43P–47P. [CrossRef]
90. Sobacchi, E.; Mesinger, A. How does radiative feedback from an ultraviolet background impact reionization? *Mon. Not. R. Astron. Soc.* **2013**, *432*, 3340 [CrossRef]
91. Diemer, B. COLOSSUS: A Python Toolkit for Cosmology, Large-scale Structure, and Dark Matter Halos. *Astrophys. J. Suppl. Ser.* **2018**, *239*, 35. [CrossRef]
92. Tinker, J.; Kravtsov, A.V.; Klypin, A.; Abazajian, K.; Warren, M.; Yepes, G.; Gottlober, S.; Holz, D.E. Toward a Halo Mass Function for Precision Cosmology: The Limits of Universality. *Astrophys. J.* **2008**, *688*, 709. [CrossRef]
93. Schneider, A.; Smith, R.E.; Reed, D. Halo mass function and the free streaming scale. *Mon. Not. R. Astron. Soc.* **2013**, *433*, 1573–1587. [CrossRef]
94. May, S.; Springel, V. He halo mass function and filaments in full cosmological simulations with fuzzy dark matter. *arXiv* **2022**, arXiv:220914886.
95. Aversa, R.; Lapi, A.; De Zotti, G.; Danese, L. Black Hole and Galaxy Coevolution from Continuity Equation and Abundance Matching. *Astrophys. J.* **2015**, *810*, 74. [CrossRef]
96. Moster, B.P.; Naab, T.; White, S.D.M. EMERGE—An empirical model for the formation of galaxies since $z\sim10$. *Mon. Not. R. Astron. Soc.* **2018**, *477*, 1822. [CrossRef]
97. Cristofari, P.; Ostriker, J.P. Abundance matching for low-mass galaxies in the CDM and FDM models. *Mon. Not. R. Astron. Soc.* **2019**, *482*, 4364–4371. [CrossRef]
98. Behroozi, P.; Wechsler, R.H.; Hearin, A.P.; Conroy, C. UNIVERSEMACHINE: The correlation between galaxy growth and dark matter halo assembly from $z = 0$–10. *Mon. Not. R. Astron. Soc.* **2020**, *488*, 3143–3194. [CrossRef]

99. Foreman-Mackey, D.; Hogg, D.W.; Lang, D.; Goodman, J. emcee: The MCMC Hammer. *Publ. Astron. Soc. Pac.* **2013**, *125*, 306. [CrossRef]
100. Kistler, M.D.; Yuksel, H.; Beacom, J.F.; Hopkins, A.M.; Wyithe, J.S.B. The Star Formation Rate in the Reionization Era as Indicated by Gamma-Ray Bursts. *Astrophys. J.* **2009**, *705*, L104. [CrossRef]
101. Gruppioni, C.; Bethermin, M.; Loiacono, F.; Le Fevre, O.; Capak, P.; Cassata, P.; Faisst, A.L.; Schaerer, D.; Silverman, J.; Yan, L.; et al. The ALPINE-ALMA [CII] survey. The nature, luminosity function, and star formation history of dusty galaxies up to $z \approx 6$. *Astron. Astrophys.* **2020**, *643*, A8. [CrossRef]
102. Schwarz, G. Estimating the Dimension of a Model. *Ann. Stat.* **1978**, *6*, 461. [CrossRef]
103. Liddle, A.R. How many cosmological parameters? *Mon. Not. R. Astron. Soc.* **2004**, *351*, L49. [CrossRef]
104. Spiegelhalter, D.J.; Best, N.G.; Carlin, B.P.; Van Der Linde, A. Bayesian measures of model complexity and fit. *J. R. Statist. Soc. B* **2002**, *64*, 583. [CrossRef]
105. Park, J.; Gillet, N.; Mesinger, A.; Greig, B. Properties of reionization-era galaxies from JWST luminosity functions and 21-cm interferometry. *Mon. Not. R. Astron. Soc.* **2020**, *491*, 3891. [CrossRef]
106. Labbe, I.; Bezanson, R.; Atek, H.; Brammer, G.; Coe, D.; Dayal, P.; Feldmann, R.; Forster Schreiber, N.M.; Franx, M.; Geha, M.C.; et al. UNCOVER: Ultra-deep NIRCam and NIRSpec Observations Before the Epoch of Reionization. *JWST Propos. Cycle* **2021**, *1*, 2561.
107. Robertson, B.E. Galaxy Formation and Reionization: Key Unknowns and Expected Breakthroughs by the James Webb Space Telescope. *arXiv* **2021**, arXiv:2110.13160.